Supplementary Materials

Confinement Induced Plastic Crystal-Crystal Transitions in Rod-Like Particles with Long-Ranged Repulsion

Bing Liu, Thijs H. Besseling, Alfons van Blaaderen, and Arnout Imhof

Soft Condensed Matter, Debye Institute for Nanomaterials Science,
Utrecht University, Princetonplein 5, 3584 CC Utrecht, the Netherlands
(Dated: February 5, 2015)

EXPERIMENTAL DETAILS

Particle Synthesis

The fluorescent silica rod-like particles were prepared by a two-step procedure. In the first step, we prepared monodisperse silica rods following a reported procedure [Ref. [24] of the main text]. 30 g of poly(vinylpyrrolidone) (PVP, Mn = 40.000, Sigma-Aldrich) was dissolved in 300 ml of 1-pentanol (99 %, Sigma-Aldrich) containing 30 ml of absolute ethanol (Baker). After PVP was dissolved, 8.4 ml of ultrapure water (18.2 MΩ), 2 ml of 0.18 M sodium citrate dihydrate (99 %, Sigma-Aldrich), and 6.75 ml of ammonia aqueous solution (25 %, Merck) were added and the flask was shaken. Afterwards, 3.0 ml of tetraethylorthosilicate (TEOS, 98%, Sigma-Aldrich) was added. The mixture was shaken and then allowed to react undisturbed for 24 h. The as-prepared silica rods were separated by centrifuge and then washed with ethanol, water and ethanol, respectively. To grow a fluorescent shell[Ref. [25] of the main text], half of the as-prepared silica rods were dispersed into 150 ml ethanol containing 10 ml of water and 12 ml of ammonia aqueous solution (25 %). Then 5 ml of a solution containing 0.8 ml TEOS, 25 mg of fluorescein isothiocyanate (FITC, isomer I, 90%, Sigma-Aldrich), and 37 μl of 3-aminopropyltriethoxysilane (APS, 99%, Sigma-Aldrich) was added. The reaction was stirred overnight. Afterwards, the silica rods were washed with ethanol for three times. To grow a non-fluorescent shell, a similar procedure was performed but without the addition of FITC and APS. The thickness of the shell was adjusted by controlling the amount of added TEOS (0.5 - 2 ml). The as-prepared colloidal rods have a three-layered structure: non-fluorescent silica core, fluorescent shell (dye: FITC, ca. 30-50 nm) and non-fluorescent shell (ca.100 nm).

In the second step, we modified the silica rods with octadecyltrimethoxylsilane (OTMOS, 90 %, Sigma-Aldrich) by an ultrasonic-assisted coating procedure [Ref. [6] of the main text]. In brief, a solution of OTMOS, butylamine (BA, 99.5 %, Sigma-Aldrich) and dried toluene (1:1:10 v/v/v) was prepared, and then 10 (wt.-)% of dried silica rods was added to this solution. The suspension was sonicated at 30∼55 °C for 4 h (Branson 2250). Afterwards, the colloidal rods were washed in turn with toluene, cyclohexane and cyclohexylchloride (CHC, 98 %, Merck). Finally, the colloidal rods were dispersed in deionized CHC for further use. The length L and diameter D of the as-prepared rods were 2.29 μm (6.0 %) and 0.60 μm (6.5 %), respectively, which corresponded to an aspect ratio 3.8. Between parentheses is the polydispersity (standard deviation divided by the mean). The rods were assumed to have the same surface potential as spherical particles with the same surface chemistry composition. The surface potential of the latter was estimated by measuring pair correlation function and subsequently fitting to classical DLVO theory [1]. The surface potential was estimated in this way to be roughly -50 mV.

Electrical conductivity measurement

We estimated the screening length by measuring the conductivity of the deionized solvent CHC with a Scientifica 627 conductivity meter. For the calculation of the ionic strength we made use of Waldens rule [2], which states that the product of the limiting equivalent conductance and the viscosity is a constant between different media, i.e. $\Lambda_0^{\text{Ethanol}}\eta_0^{\text{Ethanol}} = \Lambda_0^{\text{CHC}}\eta_0^{\text{CHC}}$. We used literature values for the limiting equivalent conductance of HCl in ethanol [3] and the viscosity of 1.5675 mPa.s at 298.15 K for CHC [4]. The Debye screening length can then be estimated by $\kappa^{-1} = \sqrt{8\pi\lambda_{\text{B}}c}$. Here, $\lambda_{\text{B}} = e^2/(4\varepsilon\varepsilon_0 k_{\text{B}}T)$ is the Bjerrum length, and ε and ε_0 are the dielectric constant of the solvent and the permittivity of vacuum. e is the elementary charge, k_{B} is Boltzmanns constant and T is the absolute temperature. A final conductivity of ca. 180 pS/cm for particle-free CHC corresponded to κ^{-1} of ca. 1.2 μm estimated with the above formula.

Sample Cell Fabrication

A wedge-shaped cell was constructed for our experiments. The cell consisted of two thin glass slides (55×24 mm, No.1, Menzel-Gläser), which were coated in turn with a fluorescent and a non-fluorescent silica layer. To grow a thin fluorescent layer, the glass slides were immersed into 150 ml ethanol containing 10 ml of water and 12 ml of ammonia aqueous solution (25 %). Then 5 ml of a solution containing 0.4 ml TEOS, 15 mg of fluorescein isothiocyanate (FITC, isomer I, 90%, Sigma-Aldrich), and 20 μl of 3-aminopropyltriethoxysilane (APS, 99%, Sigma-Aldrich) was added. The reaction was performed for 24 h. Afterwards, the glass slides were intensively washed with ethanol with the assistance of sonication. To grow a non-fluorescent shell, a similar procedure was performed but without the addition of FITC and APS. Afterwards, the surfaces of the two glass slides were grafted with the silane OTMOS. By doing this, we tried to achieve the exact same surface chemistry of the wall as compared to that of the colloidal rods. A 50 μm diameter nickel alloy wire was used as a spacer, and put on one end between the two slides. The two glass slides were then fixed with UV-sensitive glue (Norland No. 68) and one end was kept open for the filling with the suspension of rods (Figure S1). This cell allowed us to study the sample thickness up to a maximum of 50 μm. The measurement of the slit width was performed by confocal fluorescence imaging, and a conservative estimate of the uncertainty is $\pm 0.16 \mu$m. We determined that the refractive index mismatch between sample and immersion-liquid did not change the height significantly [5].
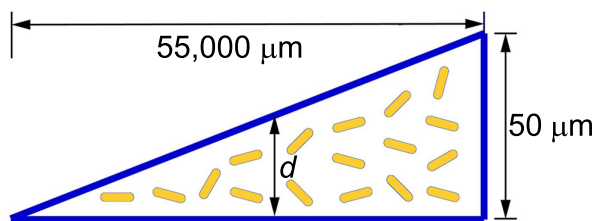

FIG. S1. Schematic illustration of rod-like particles confined in a wedge-shaped cell

Sample Preparation

The sample suspension medium was CHC. The received CHC (conductivity >1000 pS/cm) was deionized by using molecular sieves (4Å, Sigma-Aldrich) and subsequent neutral aluminium oxide (Sigma-Aldrich). After purification, CHC had a conductivity around 180 pS/cm.The suspension volume fraction we used in all experiments was 0.0026. The suspension of rods was pulled into the cell by capillary force through the open end. After the suspension had filled the whole cell, the open end was sealed with the glue. The sample was equilibrated for at least 1 hour at room temperature before observation.

Confocal Microscopy Measurements

The images and datasets were recorded with a laser scanning confocal microscope (Leica TCS SP2 or Leica TCS SP8, the latter was equipped with a 12 kHz resonant scanner). All images were taken in fluorescence mode (63×NA 1.4, immersion liquid: n_e = 1.5180, Leica). The excitation wavelength was 488 nm. For the acquisition of 2D x-y-t datasets, the scanning time used for each frame was 0.657 s, achieved by scanning 512×512 pixels with a pixel size of 155 nm. The positional coordinates of the rods were found from an averaged image over the corresponding x-y-t dataset. A conservative estimate of the uncertainty in the center of mass of a rod was less than 80 nm. For obtaining 3D x-y-z-t datasets, the scanning time of each series was 0.27 s, achieved by scanning 400×100×20 pixels with a pixel size of 115 nm in x-y and 319 nm in z, from which we obtained centers of mass and angular coordinates using a home-written computer tracking code, as explained in more detail in the following paper[Ref. 7 of the main text]. The uncertainty in the orientations is estimated to be around 27(deg) [Ref. [6] and Refs 4, 6, 7 of the main text]. Each 3D dataset had more than 6000 particles.

CRYSTAL STRUCTURES

As we mentioned in the main text and summarized in Fig. S2, Fig. S3 and Fig. S4, we analyzed the formed crystal structure by confocal microscopy. The images are obtained from x-y-z datasets by superposing the frames over around 7∼ 10 s and projecting them in x-y plane. The colors in the images show the positions of particles. Red, green, yellow and cyan are in turn for the layers from the bottom to the top.

PAIR CORRELATION FUNCTION

The pair correlation functions for monolayered region, trilayered region and tetralayered region discussed in the main text are given in Fig. S5. The pair correlation function for bilayered region is shown in Fig. 2c in the main text.
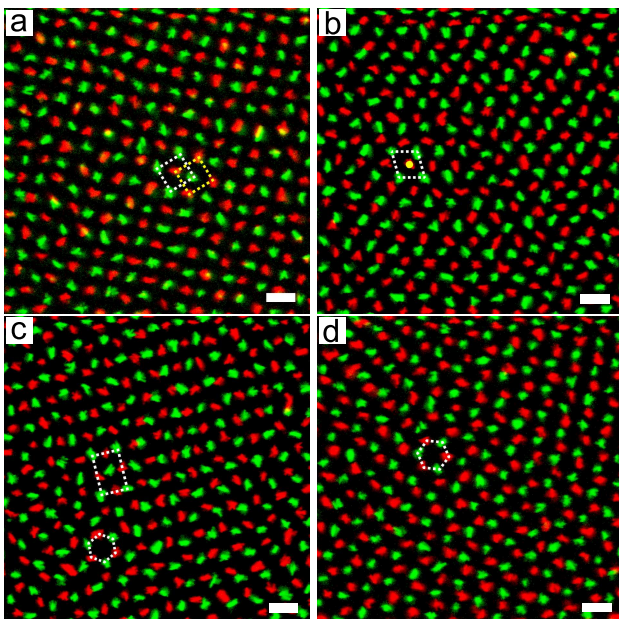
FIG. S2. Structure of bilayered crystal. a) The 2□ phase, which corresponds to Fig. 1c in the main text, shows a staggered structure with the projected position of a particle in the neighbouring layer situated in the geometric center of a primitive unit cell, marked by the two dashed squares; b) The $2R$ phase, which corresponds to Fig. 1d in main text and shows a staggered rhombic structure with the projected position of a particle in the neighbouring layer situated in the geometric center of a primitive unit cell, marked by the dashed rhombus; c) The 2△ phase, which corresponds to Fig. 1e in main text. In this case, both a staggered triangular phase marked by dashed hexagon, and the rhombic phase (R_c, see ref. 21 of the main text) marked by the dashed rectangle were observed; d) The 2△ phase, which corresponds to Fig. 1f in main text and shows a staggered triangular structure.

FIG. S3. Structure of trilayered crystal. a) The 3□ phase, which corresponds to Fig. 1g in main text, shows a staggered structure with the projected position of a particle in the neighbouring layer situated in the geometric center of a primitive unit cell, marked by the dashed square; b) The $3R$ phase, which corresponds to Fig. 1h in the main text, shows a staggered rhombic structure with the projected position of a particle in the neighbouring layer situated in the geometric center of a primitive unit cell, marked by the dashed rhombus; c) The 3△ phase, which corresponds to Fig. 1i in the main text. In this case, we observed three different packing structures: face centered cubic (FCC), marked by the dashed hexagons (top-right), hexagonal close packing (HCP), marked by the dashed hexagons (bottom-right), and the rhombic phase (R_c, see ref. 21 of the main text), marked by the dashed rectangles.

IN-PLANE ANGLE DISTRIBUTION

Fig. S6 showed the projected angle distribution of the rod orientations in x-y plane. The corresponding distributions of the z components are shown in Fig. 3a in the main text. The figures suggest that the rods have roughly random orientations in the x-y plane. The dashed lines are for a uniform distribution.

ORIENTATIONAL DISTRIBUTION

The orientational distribution of rods in trilayered region and tetralayered region mentioned in the main text are given in Fig. S7. Meanwhile, we observed an obvious difference in the orientations between the rods in the layers adjacent to the wall and the layers in the middle. As expected, the rods in the former show higher tendency to be parallel to the wall. However, this effect weakened with increasing of the slit width until the insertion of new
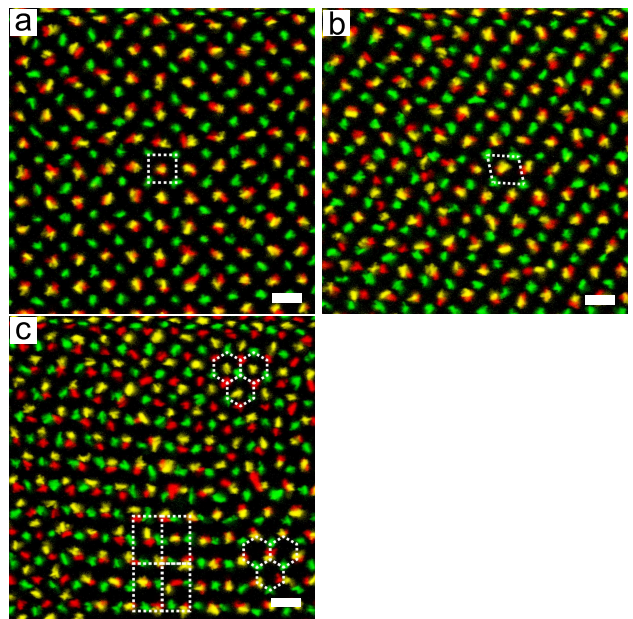
layers.

ORDER PARAMETERS

The global m-fold bond-orientational order parameter ϕ_m was defined as:

$$\psi_m = < \frac{1}{N} \sum_{\alpha=1}^{N} \frac{1}{N_b} \sum_{\beta=1}^{N_b} \exp(im\theta_{\alpha,\beta}) >$$

(S1)

where the angular brackets indicate an ensemble average, N is the number of the particles, N_b is the number of nearest neighbors of particle α, and $\theta_{\alpha,\beta}$ is the angle between a fixed reference axis and the bond joining particle α with a neighboring particle β. Here, we calculated N_b by choosing a cutoff which is based on the position of the first minimum after the first peak in the pair correlation function $g(r)$.
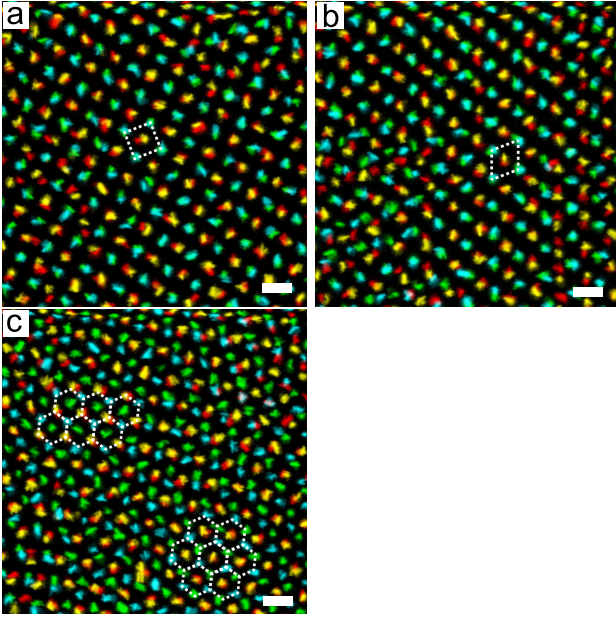
FIG. S4. Structure of tetralayered crystal. a) The 4□ phase, which shows a staggered structure with the projected position of a particle in the neighbouring layer situated in the geometric center of a primitive unit cell, marked by the dashed square; b) The 4R phase, which shows a staggered rhombic structure with the projected position of a particle in the neighbouring layer situated in the geometric center of a primitive unit cell, marked by the dashed rhombus; c) The 4△ phase. In this case, we observed both FCC and HCP. In the hexagon-marked location, the three layers close to bottom formed a HCP structure, but the three layers above the bottom layer formed an FCC structure.

The orientational order parameter S was defined as:

$$S = \tfrac{1}{2} < 3\cos^2\theta - 1 >$$

(S2)

where θ is the angle with respect to the z axis (perpendicular to the wall), and the angular brackets denote the ensemble average. S takes values form -0.5 to 1, where S = -0.5 is for rods that all have orientations perpendicular to the z axis, $S = 0$ for random orientations, and $S = 1$ for rods that are all perfectly aligned with the z axis.

ORIENTATIONAL CORRELATION FUNCTIONS

The spatial orientational correlation function was defined as:

$$g_2(r_{ij}) = < \cos(2(\theta_i - \theta_j)) >$$
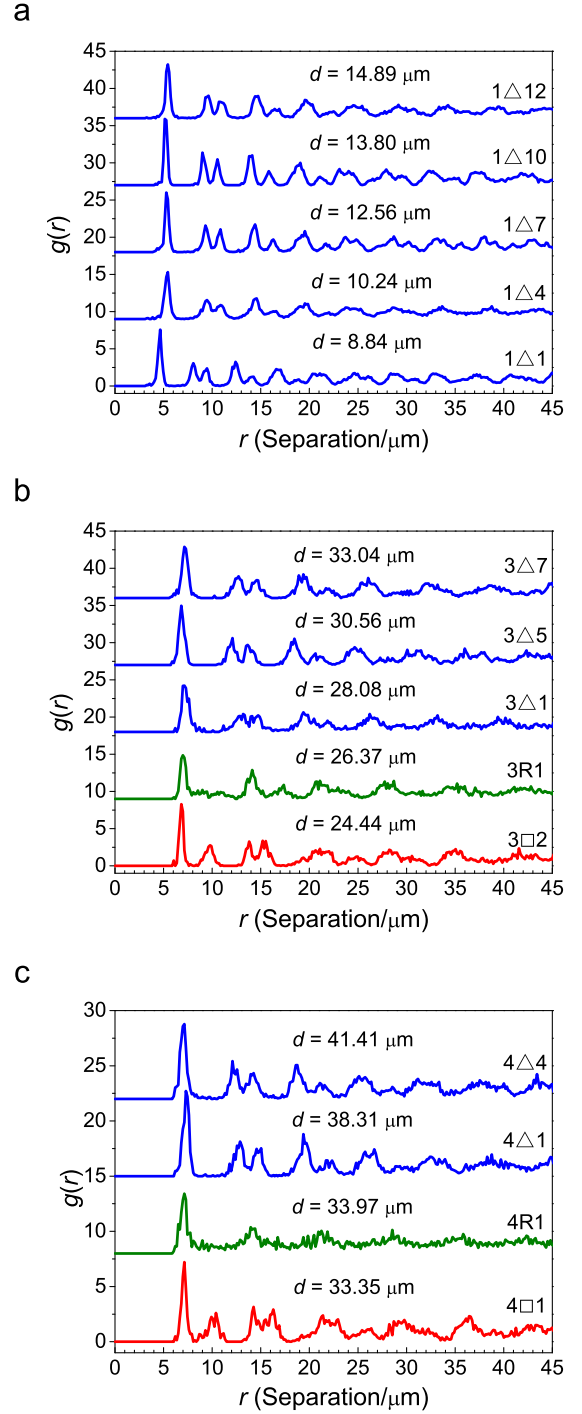
(S3)

FIG. S5. Transitions in crystal lattice versus slit width. a-c) Pair correlation functions in the monolayer regions (a), the trilayer region (b) and the tetralayer region (c), respectively, calculated from the averaged positions of the centers of mass of the rods over 81.75 s.
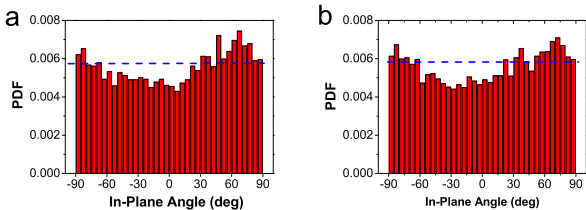
FIG. S6. The in-plane angular distributions of rods. a) sample 1△1 and b) sample 1△4.
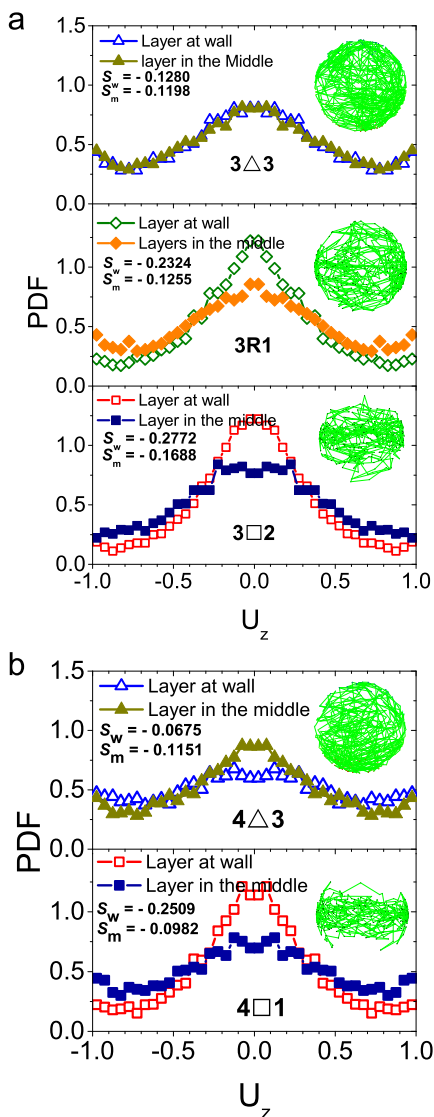

FIG. S7. Orientational distributions. A comparison of the distributions of the z components of the orientations between rods in the layers adjacent to the wall and rods in middle layers. a) In the trilayer region and b) in the tetralayer region. The symbols □, R, and △ in the figures denote square, rhombic and hexagonal lattices, respectively. Insets show the corresponding rotational trajectories of a single rod.

where the angular brackets denote the ensemble average, and $\theta_{i,j}$ are the angles between a fixed reference axis and the orientations of particles i and j, which are separated by a distance r_{ij}. The time-dependent orientational autocorrelation function was defined as:

$$C_2(t) = \tfrac{1}{2} < \tfrac{1}{N} \sum_{i=1}^{N} 3[\mathbf{u}_i(0) \cdot \mathbf{u}_i(t)]^2 - 1 >$$

(S4)

where N is the number of the particles in the system, $\mathbf{u}_i$ is the unit vector that defines the orientation of particle i, and the angular brackets denote the ensemble average. The $C_2(t)$ of rods in the bilayer region, trilayer region and tetralayer region mentioned in the main text are given in Fig. S8.
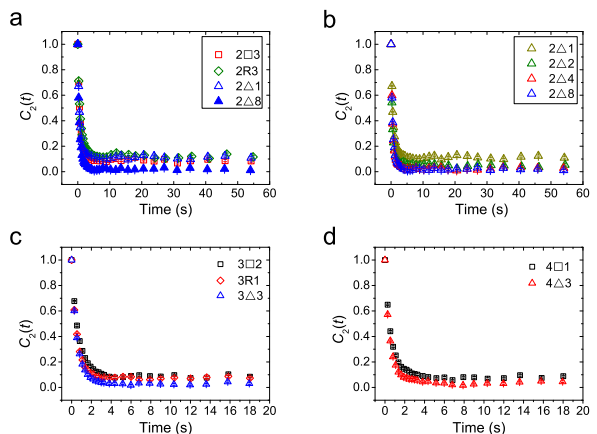

FIG. S8. The time-dependent orientational auto-correlation functions of rods. a,b) In the bilayer region, c) In the trilayer region and d) in the tetralayer region. The symbols □, R, and △ in the figures denote square, rhombic and hexagonal lattices, respectively. The curves decay quickly to small positive values illustrating that the rods quickly explore most but not all of the orientational space.

CALCULATION MODEL

Though the interaction potential between two charged spherical particles in suspension media is well described by the Yukawa potential, the repulsive electrostatic part of the Derjaguin-Landau-Verwey-Overbeek (DLVO) theory, the interaction potential between two anisotropic particles e.g. charged rods with short-ranged potential is not analytically known [7]. As an approximation, a so-called Yukawa segment model has been extensively used to describe the interaction between two charged rods in simulation and theory [Refs. 29-31 of the main text]. In this model, one rod is divided into n equal segments, and on each segment the amount of charge is equal to Q/n

$(Q = ze$, denotes the total charge of a rod). For each segment, a point-like Yukawa potential is then used. In this model, the interaction between the pth rod and the qth rod is thus given by a sum over all pairs of segments lying on different rods (Fig. S9):
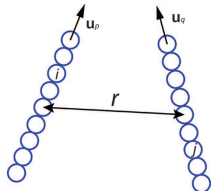

FIG. S9. Schematic model.

$$U_{pq}(r) = U_0 \sum_{i,j=1}^n \frac{\exp(-\kappa r_{ij})}{\kappa r_{ij}}$$

(S5)

where the prefactor U_0 is given by:

$$U_0 = \left(\frac{z}{n}\right)^2 \frac{e^2 \kappa}{4\pi \varepsilon \varepsilon_0} \left(\frac{\exp(\kappa a)}{1+\kappa a}\right)^2$$

(S6)

and the interrod segment distance is given as

$$r_{ij} = |r_p - r_q + \mathbf{u}_p d_n(2i-1-n)/2 - \mathbf{u}_q d_n(2j-1-n)/2|$$

(S7)

d_n is the distance between two neighboring segments. In order to adjust the quadrupolar moment of this model to that of a homogenously charged rod of length L and charge Q, d_n is given by:

$$d_n = L/\sqrt{(n+1)(n-1)}$$

(S8)

This is just an approximate model due to the absence of correlations between counter ions and the correlation between counter ions and charges belonging to different segments, and is moreover only justified for a diluted and weakly screened system [Refs. 29-31 of the main text]. However, our system has a large screening length and shows large interrod distances $(r/L > 2)$, and thus we also expect this model to capture most of the physics and hope that the deviations which go beyond the present paper will not change our main conclusions. In addition, because here we care more about a comparison of the

repulsive potentials between rods with different orientations than an absolute value of the potential, we believe that this makes it less likely that deviations from a full calculation will not influence our main conclusions.

Now the interaction potential between any two rods with a center-center separation r can be calculated. As in experimental observations the rods were restricted to lattice sites and so two neighboring rods were kept at a fixed separation r, as there were hardly measurable density differences. However, their rotational motion was much less restricted. Therefore, the interaction potential between two rods will vary depending on their orientations. To simplify the calculation, a reasonable method is taking an average over all allowed orientations of the two rods. In a crystal lattice, every rod will have the same environment and be subject to the same constraints. If one rod has m possible orientations, then the averaged interaction is given by:

$$U_{pq,\mathrm{avg}}(r) = \frac{1}{m^2} \sum_{p,q=1}^m U_{pq}(r, \mathbf{u}_p, \mathbf{u}_q)$$

(S9)

Similarly, the interaction potential $W(h)$ between the pth rod and the wall is described as:

$$W_p(h) = W_0 \sum_{l=1}^N \exp(-\kappa h_l)$$

(S10)

where l denotes the lth segment, and h denotes the separation between the center of mass of the segment and the wall, and the prefactor W_0 is given by [8]:

$$W_0 = 4\pi\varepsilon\varepsilon_0 \varphi_{\mathrm{w,eff}} \varphi_{\mathrm{r,eff}} a$$

(S11)

with φ_{w}, φ_{r} denote the effective surface potential of the wall and the rod, respectively, and are expressed as:

$$\varphi_{\mathrm{w,r,eff}} = 4\frac{k_{\mathrm{B}}T}{e}\tanh\left(\frac{e\varphi_{\mathrm{w,p}}}{4k_{\mathrm{B}}T}\right)$$

(S12)

This is then also averaged over orientations of the rods, similarly to eq. (S9).

$$W_{p,\mathrm{avg}} = \frac{1}{m} \sum_{p=1}^m W_p(h, \mathbf{u}_p)$$

(S13)

Calculation of total repulsive potential of one rod on a perfect lattice confined between walls: For a single rod on a lattice the most probable orientation is the one that minimizes the potential energy of its interactions with the other rods and with the walls. For a collection of N rods, the total repulsive potential energy of the system thus can be described as a sum of the repulsive potential over N particles:

$$U_{\text{tot}} = \sum_{p,q=1\ p<q}^{N} U_{pq,\text{avg}} + 2 * \sum_{p=1}^{N} W_{p,\text{avg}}$$

(S14)

In a screened environment, one rod has an anisotropic potential due to finite-size double layer. Moreover, in a wedge-shaped confinement the rods possibly do not explore all orientations, so the total repulsive potential U_{tot} is orientation- (distribution) dependent. Therefore, by finding the minimum U_{tot} we can find the preferred orientation distribution of the rods. Again, we assume that every rod is in the same average environment (for example in a perfect crystal), so to compare the total repulsive potential U_{tot} can be simplified to the averaged repulsive potential U_{s} over N rods, which is given by:

$$U_{\text{s}} = \frac{U_{\text{tot}}}{N} = \sum_{q}^{\frac{N-1}{2}} U_{pq,\text{avg}} + 2 * U_{p,\text{avg}}$$

(S15)

U_{s} is still orientation-(distribution) dependent. Because the electrostatic potential decays dramatically with the interrod distance as shown in Fig. S10, the contribution from the second neighbors is 1~2 orders of magnitude lower than that from the nearest neighbors (See Fig.2c in the maintext and Fig.S5 for the separation between a rod and its neighbours). Therefore, we consider only the first nearest neighbors for the calculation of U_{s}.

The values of the parameters used in our calculations Surface charge $z = 239$ e (Used in equation S9 and S13); Screening length $\kappa^{-1} = 1.2$ μm; Segmental number $n = 4$; Effective surface potential of the wall (50 mV) (Used in equation S13);

In the following, we first consider the dependence of the potential energy of the rods on the orientational distribution using a distribution that is uniform within a given angular range. Then, we calculate the energy using the measured distribution obtained from our real space measurement.

In Supplementary Fig. S11 and S12, we show that the interaction potential between two rods or between a wall and a rod is dependent on the orientations of the rods, and those differences in energy range up to 1 $k_{\text{B}}T$. However, for a single rod, the effects of the repulsive potential from the neighbouring rods and from the wall are
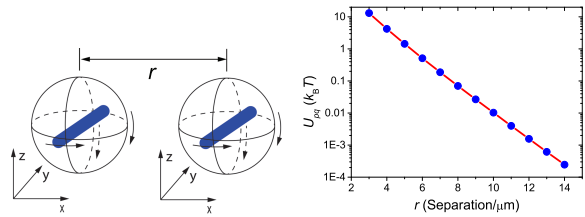

FIG. S10. Interaction potential between two freely rotating rods with random orientational distribution as a function of interrod distance r.
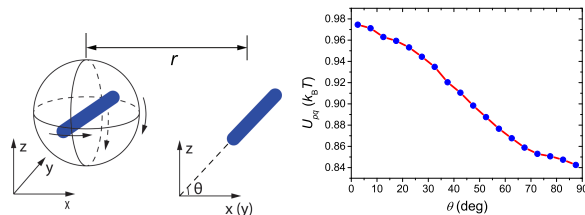

FIG. S11. Interaction potential between one freely rotated rod in x-y-z space and another rod at a fixed angle θ from x-y plane. r is fixed to 5.42 m.
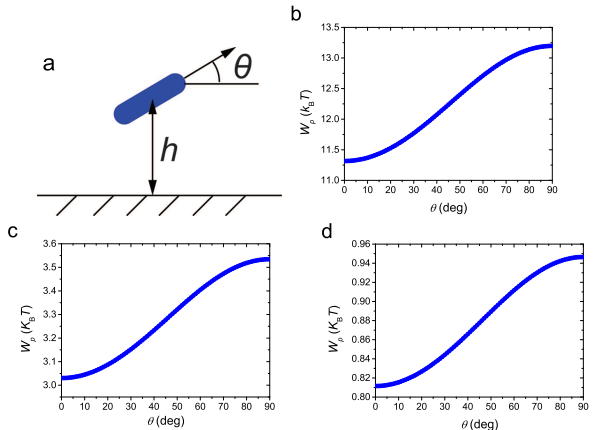

FIG. S12. Interaction potential between a wall and a rod with a fixed angle from the x-y plane. a) Schematic model. The curves at three different wall-wall separations are shown in b, c, d). b) $d = 8.8$ μm; c) $d = 11.9$ μm; d) $d = 15.0$ μm.

opposite. The repulsive potential from the neighbouring rods tends to drive the rod to be perpendicular to the wall (Supplementary Fig. S11), but that from the walls tends to drive the rod to be parallel to the wall (Fig. S12). This implies that the preferred orientation for one rod would be that direction, in which the rod has the minimum sum U_{s} of the two repulsive potentials. The calculated results are shown in Fig. S13 for the hexagonal lattice in which each rod has six nearest neighbours. Clearly, under strong confinement, the rods rotating only in the x-y plane have the minimum U_{s}, while under weak confinement the rods taking an orientation perpendicular
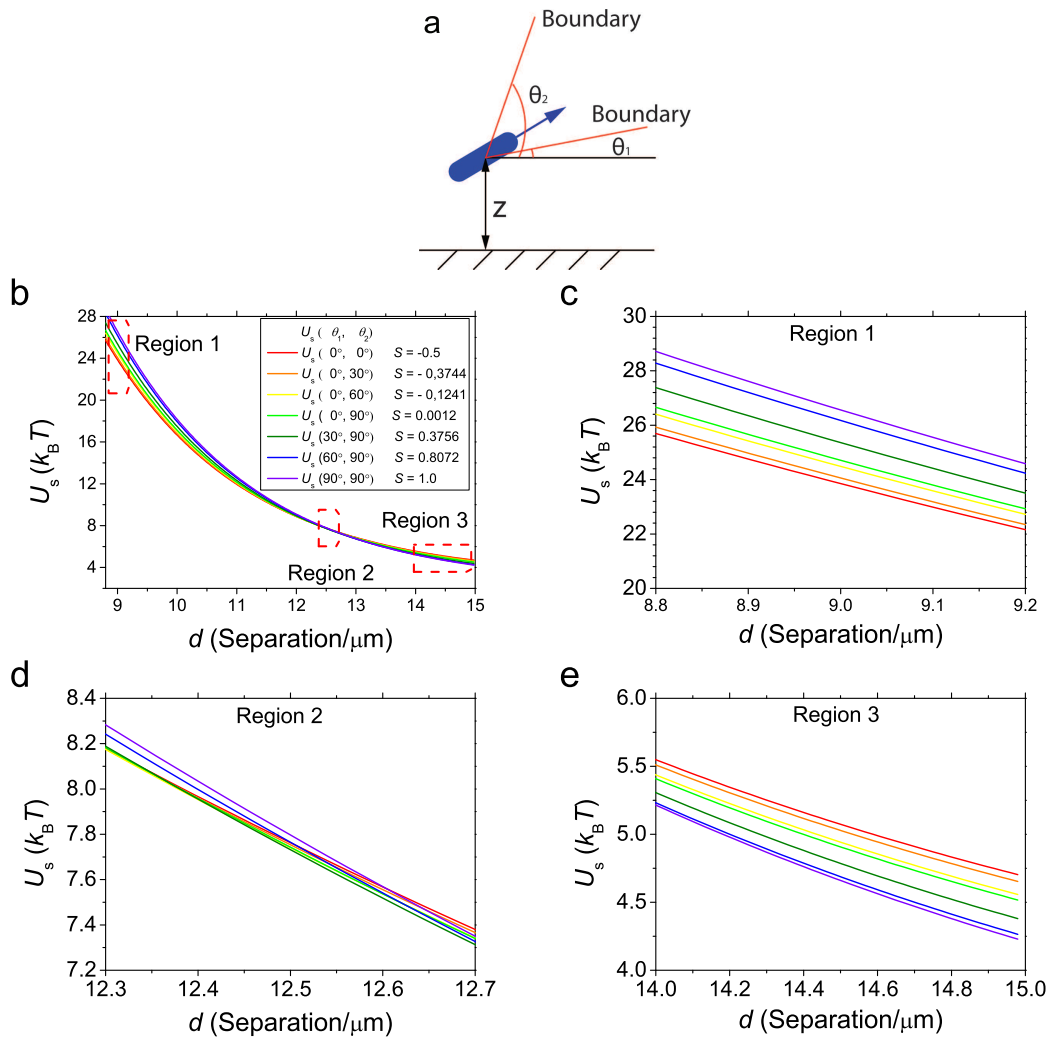
FIG. S13. The averaged potential energy U_s in a confined hexagonal lattice as a function of slit width d. a) The schematic model for the rod in confinement. θ_1, θ_2 are the two boundaries of the angular range that the rods are allowed to explore with uniform probability. b) The comparison of U_s between rods restricted to different angular ranges. Magnifications of region 1 (c), region 2 (d), and region 3 (e).

to the wall have the minimum U_s. In the intermediate confinement, there is no obvious interaction potential energy difference, so the rods can take any orientation with equal probability. The results are in agreement with our experimental observations. In experiments, the rods always assume a distribution that differs from uniform. To reduce the error from this deviation, we also calculated the U_s by selecting orientations from the measured orientational distribution and the results are shown in Fig. 4 in the main text.

In the following, we extend this model to bilayer region. Here, interactions of a given particle with one wall, the neighbours lying in the same layer, and neighbours lying in the second layer were considered. Similar to the calculations in the monolayer region, we generated three orientational distributions based on two angles θ_1 and θ_2 with the x-y plane, between which the rods are allowed to

freely rotate (see Supplementary Fig. S14a). The three distributions are $[0°, 30°]$, $[0°, 90°]$ and $[60°, 90°]$ and describe rods that have preferred orientations parallel to wall, totally random and perpendicular to the wall, respectively. The results are shown in Supplementary Fig. S14b-d and illustrate that in the whole range in which 2 □ and 2R exist orientations parallel to the wall should be preferred, whereas in the range of 2△ the rods should prefer first to be parallel to the wall at small slit width, then gradually to become randomly oriented with unrestricted rotation, and finally to orient perpendicular to the wall at larger slit width until the insertion of a new layer. This prediction exactly reproduces the sequence that is observed in the experiments.
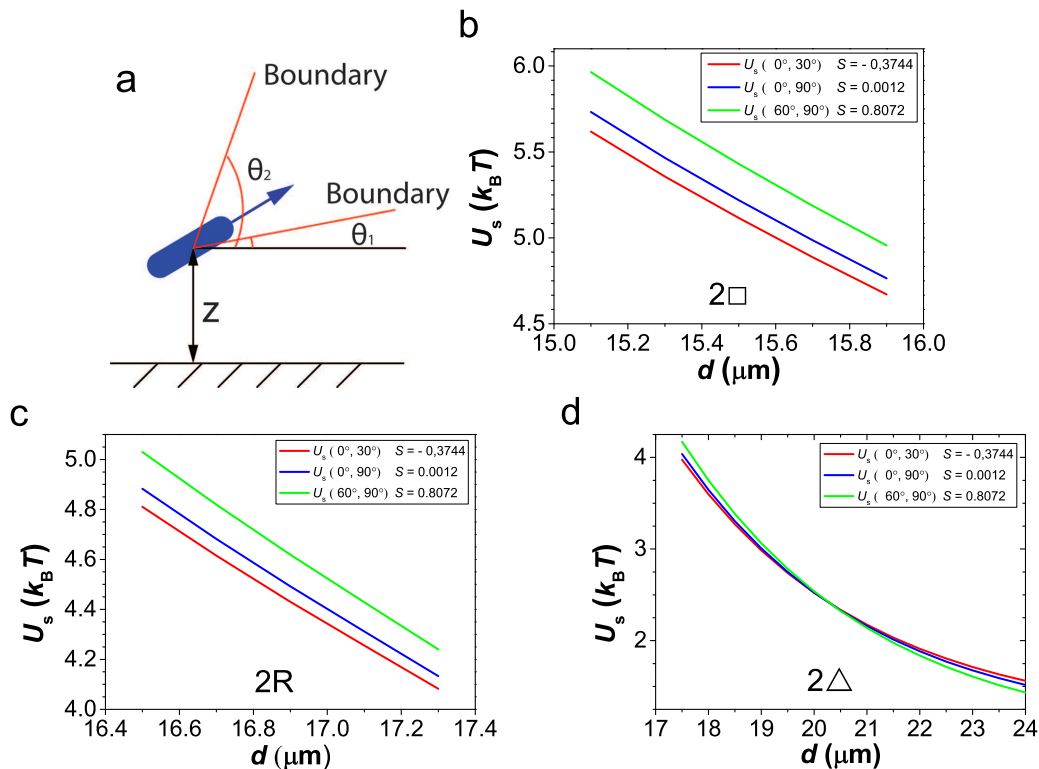
FIG. S14. The averaged potential energy U_s in a confined crystal lattice as a function of slit width d. a) The schematic model for the rod in confinement. θ_1, θ_2 are the two boundaries of the angular range that the rods are allowed to explore with uniform probability. b-d) The comparison of U_s between rods restricted to different angular ranges in the region of $2\square$ (b), $2R$ (c) and $2\triangle$.

LEGEND FOR SUPPLEMENTARY MOVIES

Supplementary Movie S1: Monolayered triangle phase. This movie, corresponding to Fig. 1a in the main text, shows a quasi-two-dimensional plastic crystal with the rods showing strong tendency to freely rotate in x-y plane. The movies is played at 10 times of real speed.

Supplementary Movie S2: Monolayered triangle phase. This movie, corresponding to Fig. 1b in the main text, shows a monolayered plastic crystal with the rods tending to freely rotate in full three dimensions. The movies is played at 10 times of real speed.

Supplementary Movie S3: Monolayered triangle phase. This movie, corresponding to Fig. 1c in the main text, shows a monolayered crystal with rods showing strong tendency to have their orientations along the direction which is perpendicular to the confining wall. The movies is played at 10 times of real speed.

Supplementary Movie S4: Bilayered square phase. This movie, corresponds to Fig. 1d in the main text, shows a bilayered plastic crystal with square symmetry, where the rods show weak tendency to freely rotate in x-y plane. The movies is played at 10 times of real speed.

Supplementary Movie S5: Bilayered rhombic phase. This movie, corresponds to Fig. 1e in the main text, shows a bilayered plastic crystal with rhombic symmetry, where the rods show weak tendency to freely rotate in x-y plane. The movies is played at 10 times of real speed.

Supplementary Movie S6: Bilayered triangle phase. This movie, corresponding to Fig. 1f in the main text, shows a bilayered plastic crystal with trianglar symmetry, where the rods show weak tendency to freely rotate in x-y plane. The movies is played at 10 times of real speed.

Supplementary Movie S7: Bilayered triangle phase. This movie, corresponding to Fig. 1g in the main text, shows a bilayered crystal with trianglar symmetry, where the rods show weak tendency to have their orientations along the direction which is perpendicular to the confining wall. The movies is played at 10 times of real speed.

Supplementary Movie S8: Tetralayered square phase. This movie shows a tetralayered plastic crystal with square symmetry. The movies is played at 10 times of real speed.

Supplementary Movie S9: Tetralayered triangular phase. This movie shows a tetralayered plastic crystal with trianglar symmetry. The movies is played at 10 times of real speed.

[1] S. H. Behrens and G. G. David, Phys. Rev. E **64**, 050401 (2001).

[2] A. Yethiraj and A. van Blaaderen, Nature **421**, 513 (2003).

[3] G. J. Jan and S. S. Danyluk, Chem. Rev. **60**, 209 (1960).

[4] S. Rodríguez, C. Lafuente, P. Cea, F. M. Royo, and J. S. Urieta, J. Chem. Eng. Data **42**, 1285 (1997).

[5] T. H. Besseling, J. Jose, and A. van Blaaderen, J. Microsc. (2014), accepted.

[6] T. Savin and P. S. Doyle, Biophys. J. **88**, 623 (2005).

[7] E. Eggen, M. Dijkstra, and R. van Roij, Phys. Rev. E **79**, 041401 (2009).

[8] J. N. Israelachvili, *Intermolecular and surface forces* (Academic Press: Waltham, MA, 2011).